Journal of Nuclear Materials 392 (2009) 280–285

Contents lists available at ScienceDirect

Journal of Nuclear Materials

journal homepage: www.elsevier.com/locate/jnucmat

Transmission electron microscopy of oxide development on 9Cr ODS steel in supercritical water

A.D. Siwy [a,*], T.E. Clark [b], A.T. Motta [a]

[a] *Department of Mechanical and Nuclear Engineering, 227 Reber Building, The Pennsylvania State University, University Park, PA 16802, USA*
[b] *Materials Research Institute, 195 Materials Research Institute Building, The Pennsylvania State University, University Park, PA 16802, USA*

ABSTRACT

Oxide layers formed on 9Cr oxide dispersion strengthened ferritic steel alloys during exposure to 600 °C supercritical water for 2- and 4-weeks were examined using cross-sectional transmission electron microscopy. A focused ion beam *in situ* lift-out technique was used to produce site-specific samples with electron transparent areas up to 8 µm by 10 µm. The oxide layers consist of several sub-layers: an Fe-rich outer oxide, a Cr-rich inner oxide, and a diffusion layer, extending beyond the oxide front into the metal. An evolution of the oxide layer structure is seen between 2 and 4 weeks, resulting in the development of a band of Cr_2O_3 at the diffusion layer/metal interface from the previously existing continuous mixture of $FeCr_2O_4$ 'fingers' and bcc metal. It is believed that transport in this Cr_2O_3 layer at the diffusion layer/metal interface becomes the rate-limiting step for oxide advancement, since this change in oxide structure also corresponds to a decrease in corrosion rate.

1. Introduction

The supercritical water reactor (SCWR) is one of the Generation-IV nuclear reactor concepts, currently being studied to help meet future demands for efficient and safe energy production. The operating conditions of the SCWR provide new material challenges for many reactor components, including fuel cladding. Potential candidates for fuel cladding include austenitic stainless steels, solid solution and precipitation-hardened alloys, ferritic–martensitic alloys, and oxide dispersion-strengthened alloys (ODS) [1]. While austenitic alloys undergo cracking, uniform corrosion is a major concern for ferritic steel fuel cladding in the SCWR. The focus of this study is on the ferritic–martensitic 9Cr ODS steel, which was originally developed by JAEA for use in sodium-cooled fast reactors [2].

Previous investigations performed on oxide layers developed on this steel during exposure to 360, 500, and 600 °C supercritical water (SCW) [3,4] have shown that the oxidation is temperature-dependent and that with increased exposure time the oxide structure becomes increasingly porous. The oxide layers consisted of an outer Fe_3O_4 magnetite layer, an inner $(Fe,Cr)_3O_4$ spinel layer, and a mixture of ferrite, spinel, and a minor phase (Cr_2O_3) in the diffusion layer. Additionally, they found a ~1 µm thick, continuous Cr-rich $(Fe,Cr)_3O_4$ band at the diffusion layer/metal interface developed in 600 °C SCW. A recent microbeam synchrotron radiation study of the oxide developed on 9Cr ODS steel exposed to 600 °C SCW has found that this band has a diffraction pattern consistent with that of Cr_2O_3 [5].

The purpose of this study is to investigate the development of the oxide formed on 9Cr ODS steel, and in particular, to examine the changes with exposure time in the structure of the diffusion layer that forms ahead of the oxide front. Mechanistic understanding of the role played by the oxide layer structure in reducing corrosion may aid in the development of alloys which exhibit superior corrosion resistance in SCW.

2. Experimental methods

The 9Cr ODS steel was fabricated by JAEA and corrosion tested in SCW at the University of Wisconsin (UW). Coupon specimens were normalized at 1050 °C for one hour, air cooled, then tempered at 770 °C for two hours before a final air cooling. Further details of their fabrication can be found elsewhere [2]. The chemical composition of the steel is listed in Table 1.

Samples were exposed to supercritical water at 600 °C and 25 MPa in a natural circulation corrosion loop at UW. The UW-SCW loop is made of Inconel 625 and has a flow velocity of 1 m/s and a mass flow rate of 0.4 kg/s [6].

Samples were examined using scanning electron microscopy (SEM) and transmission electron microscopy (TEM). The SEM

---

* Corresponding author. Tel.: +1 814 865 0036; fax: +1 814 865 8499.
E-mail address: andrew.siwy@psualum.com (A.D. Siwy).

0022-3115/$ - see front matter © 2009 Elsevier B.V. All rights reserved.
doi:10.1016/j.jnucmat.2009.03.032

Table 1
As-received chemical composition of 9Cr ODS steel listed in wt% with balance iron.

Cr	Si	Ni	Mn	C	O	P	S	Ti	Y	W
8.6	0.048	0.06	0.05	0.14	0.14	<0.05	0.003	0.21	0.28	2

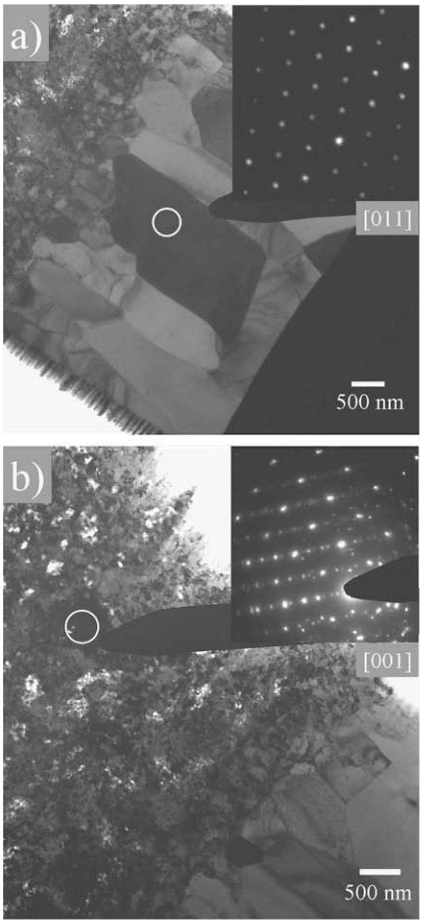

Fig. 2. TEM BF images and corresponding diffraction patterns indexed as (a) the Fe_3O_4 zone axis [0 1 1], from an outer oxide grain and (b) the $FeCr_2O_4$ zone axis [0 0 1], from the inner oxide of the 4-week 9Cr ODS steel sample.

used was a FEI Quanta 200 ESEM. The sample preparation for examination involved slicing slabs from the corrosion coupons, sliding them into slotted molybdenum rods, soaking them in epoxy, and fitting them into 3 mm brass rods [7,8]. This procedure helped ensure oxide layer stability during the polishing process. Disks were cut from the rods and finely polished for cross-sectional viewing of the oxide layer.

TEM samples were prepared via the *in situ* lift-out method [9] using a FEI Quanta 200 3D Focused Ion Beam (FIB). The samples were thinned at an ion beam voltage of 30 kV with the current dropping from 7 nA to 30 pA during the process. This approach was employed instead of traditional mechanical thinning with ion milling to produce specimens from specific locations within the oxide sub-layers, more electron-transparent area, and greater reproducibility [9].

TEM imaging, diffraction analysis, and spot energy dispersive spectrometry (EDS) were performed using a 120 kV Philips EM420 TEM. EDS maps were obtained on a 200 kV field-emission JEM 2010F TEM/STEM with an energy dispersive spectrometer. Energy filtered (EF) imaging was performed on a 200 kV LaB_6 JEOL 2010, equipped with a Gatan Tridiem^{TM} energy filter. The energy-filtered Fe and O maps were acquired via the three-window background subtraction method from the Fe–L and O–K edges [10]. This method involves acquiring a set of three energy-filtered images by placing ~30 eV windows around the pre- and post-edges. Two pre-edge images are employed for background subtraction. The acquisition time for each energy filtered image is 60 s. This technique, however, is not suitable for acquisition of energy-filtered Cr images because of the presence of the O–K edge in the Cr–L background, which prohibits accurate background subtraction. Hence, Cr–K EDS maps, for which there is no overlap with O (or Fe) were employed. In a parallel study, these oxides were also examined using microbeam synchrotron radiation diffraction and fluorescence at the Advanced Photon Source (APS) at Argonne National Laboratory [5,8].

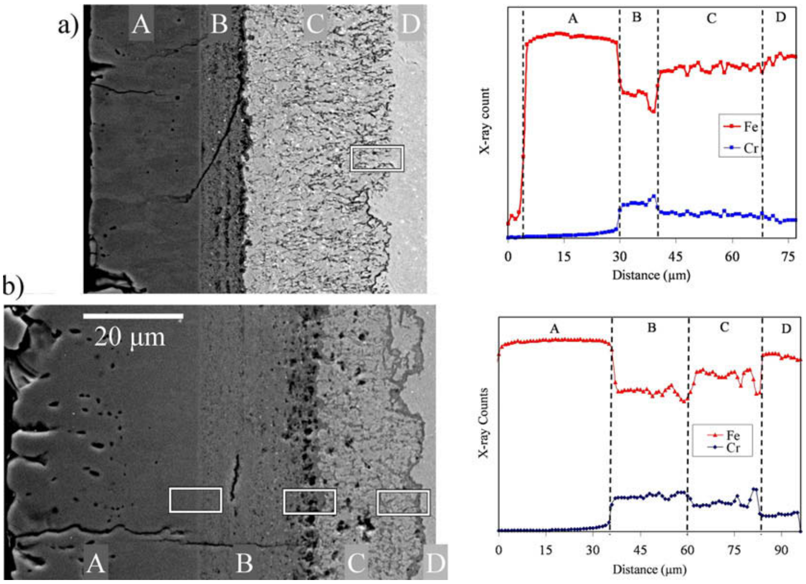

Fig. 1. SEM cross-sectional images and corresponding microbeam synchrotron fluorescence of counts associated with iron and chromium $K_{\alpha1}$ peaks versus distance in the oxide layers of 9Cr ODS steel formed during (a) 2-week [7] and (b) 4-week [5] exposures to 600 °C SCW. Both images are at the same magnification. The lettering on the SEM image and the graphs correspond as follows. A: outer oxide layer, B: inner oxide layer, C: diffusion layer, and D: base metal. The boxes indicate location of TEM samples.

3. Results and discussion

3.1. SEM examinations

Oxide layer samples on 9Cr ODS steel formed during 2- and 4-week exposures in 600 °C SCW were examined to study the evolution of the oxide layer (particularly the internal oxidation sub-layer). Fig. 1 shows a pair of SEM images taken from the two samples. Three distinct sub-layers are seen at both stages: an outer oxide (A), an inner oxide (B), and diffusion layer (C), in addition to the base metal (D). The thicknesses of these layers are 22, 9, and 29 μm (total of 60 μm), respectively, for the 2-week sample and 36, 20, and 20 μm (total of 72 μm), respectively, for the 4-week sample. The overall oxide thickness has not varied much between 2 and 4 weeks, and most of the change is in the outer layer. The sum of thicknesses of the diffusion layer and the inner oxide (~40 μm) is nearly constant, but the ratio of the two thicknesses changes, from 1:3 at 2 weeks to ~1:1 at 4 weeks. Additionally, a fully developed dark band can be seen at the diffusion layer/metal interface on the 4-week sample, while the 2-week sample shows only partially developed band segments at the diffusion layer/metal interface (bottom of figure).

Fig. 1(a) also shows a fluorescence plot obtained using microbeam synchrotron radiation. The iron and chromium $K_{\alpha1}$ counts are plotted versus distance [5] within the entire oxide layer and part of the metal layer of the 2-week 9Cr ODS steel sample. The fluorescence profile shows a step increase in chromium concentration at the inner oxide/outer oxide interface with a corresponding decrease of iron relative to the base metal, but no step increase in the diffusion layer-metal interface. The outer oxide layer is composed only of iron and oxygen. Synchrotron radiation diffraction, which can distinguish between the diffraction peaks associated with the $FeCr_2O_4$ and Fe_3O_4 phases, reveals that the diffusion layer is composed of bcc Fe and $FeCr_2O_4$. Fe_3O_4 was not detected in the diffusion layer, in agreement with previous work [8].

The corresponding plot of microbeam synchrotron radiation fluorescence from the 4-week sample (Fig. 1(b)) reveals step increases in Cr concentration at the outer oxide/inner oxide interface and at the inner oxide/diffusion layer interface but also at the diffusion layer/metal interface. The iron and chromium are inversely correlated such that the diffusion layer is depleted in iron compared to the base alloy.

The overall interpretation of these observations is that the original metal surface is coincident with the inner oxide/outer oxide

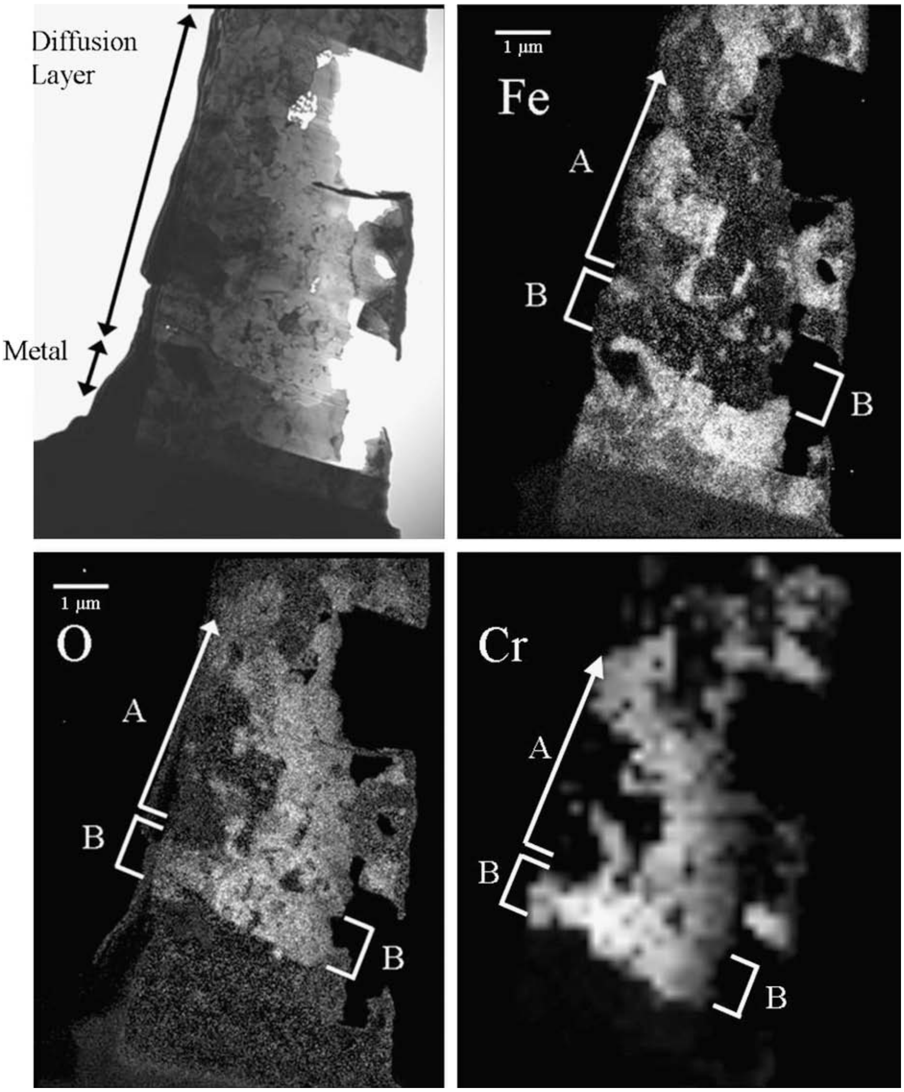

Fig. 3. TEM bright field image and corresponding Fe, O, and Cr elemental maps from diffusion layer of 9Cr ODS steel exposed at 600 °C for 4-weeks. The Cr EDS map is approximately at the same scale as the other two maps.

interface, and that the outer layer is formed by outward migration of Fe atoms from the inner and diffusion layers as well as from the base metal. The diffusion layer is formed by oxygen diffusion into the metal ahead of the oxide front. When the solubility limit of oxygen in the alloy is exceeded precipitation occurs, and thus the limit of the diffusion layer corresponds simply to the place where precipitation can occur, and more oxygen likely lies ahead of the diffusion layer/metal interface. Because Cr and Fe relocation within the layers occurs as a result of preferential oxidation, in its absence there is no gradient in Cr or Fe concentrations which is why there is no step Cr concentration at the diffusion layer/metal interface of the oxide layer present after 2 weeks. When a Cr_2O_3 layer forms, this then becomes a barrier to oxygen migration resulting in the step in Fe and Cr concentration at the diffusion layer/metal interface seen in the 2-week sample.

3.2. TEM examination

A TEM specimen was prepared from the metal/diffusion layer interface in the 2-week sample as shown in Fig. 1(a). TEM specimens were also prepared from the interfaces in the 4-week sample at locations shown in Fig. 1(b).

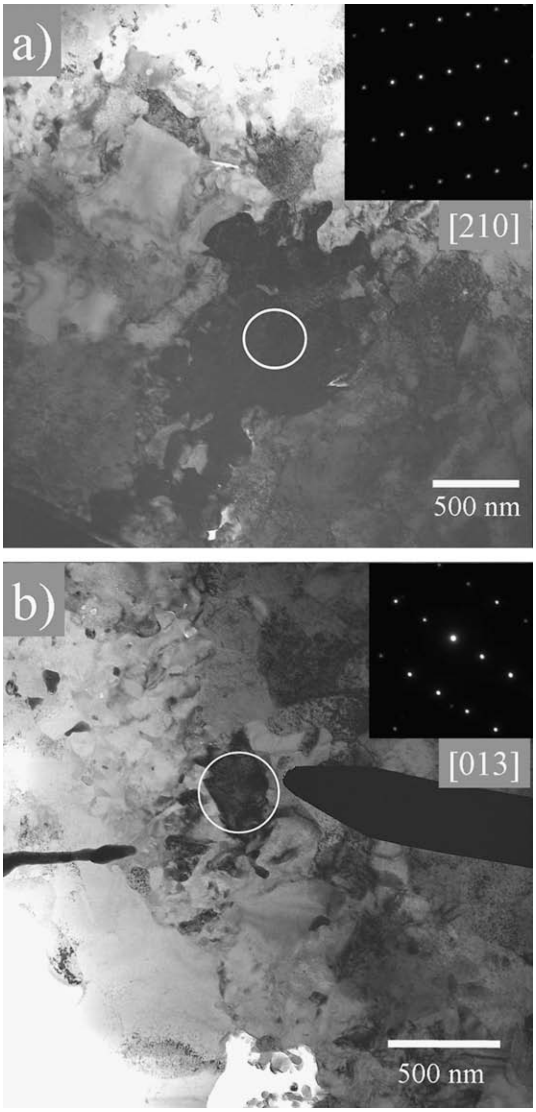

Fig. 4. TEM bright field images and corresponding diffraction patterns of (a) Cr_2O_3 with zone axis of [2 1 0] and (b) $FeCr_2O_4$, with zone axis [0 1 3], within the diffusion layer of 9Cr ODS steel after 4-week exposure.

3.2.1. 9Cr ODS steel 4-weeks

Fig. 2(a) shows a cross-sectional bright field image of the large grains of the outer oxide layer (a few microns in width). The corresponding diffraction pattern (inset) was indexed as the Fe_3O_4 [0 1 1] zone axis. It should be noted that the phases $FeCr_2O_4$ and Fe_3O_4, often reported in oxide layers formed on ferritic–martensitic alloys, exhibit the same crystal structure with only a small difference in lattice parameter, which is nearly indistinguishable via electron diffraction. In this case, we distinguish between the two phases with the elemental information from EDS.

Fig. 2(b) is a bright field image of the small grains of the inner oxide layer and the corresponding diffraction pattern indexed as the $FeCr_2O_4$ [0 0 1] zone axis. Although the inner oxide grains are smaller than the diffraction aperture, and many grains are in diffraction condition, a single crystal pattern is observed, indicating that many grains have similar orientations. EDS spectra, taken from the outer oxide layer and the inner oxide layer, confirm that the inner oxide is rich in Cr (via Cr–K) while the outer oxide contains only Fe and O.

The elemental distribution in the diffusion layer is more complex than in the other layers. As a result, EF and EDS elemental maps were employed. Fig. 3 is a bright field TEM image of the diffusion layer/metal interface and corresponding Fe (EF), O (EF), and Cr (EDS) elemental maps. The bright field image shows the sample to be thicker on one side and shows damage caused by sample preparation. The Cr_2O_3 band corresponds to the bracketed region marked 'B'. The maps reveal that this region contains Cr and O and little Fe. The remainder of the diffusion layer is marked 'A'. The chromium and oxygen are strongly correlated, whereas the iron appears to be inversely correlated to the chromium and oxygen. This indicates that the chromium oxidizes preferentially to iron, as would be expected. The elemental maps also reveal a band rich in Cr and O with some Fe-rich regions below the diffusion layer. Hence this band appears to be a two-phase mixture of mainly Cr oxide and small Fe-rich regions (likely Fe metal).

Fig. 4 shows bright field images and diffraction patterns taken from grains within this band. Fig. 4(a) (inset) is a diffraction pattern from the grain shown and was indexed as [2 1 0] Cr_2O_3. Fig. 4(b) shows a bright field image from another grain in the region in the diffusion layer adjacent to the Cr_2O_3 grains at the oxide front along with its diffraction pattern. This pattern was indexed as the spinel structure of $FeCr_2O_4$ and was one of many found trailing the Cr_2O_3 band. Cr_2O_3 and $FeCr_2O_4$ diffraction peaks were also found in the same locations in this sample via microbeam synchrotron diffraction analysis [5]. In the remainder of the diffusion layer, a mixture of Cr-rich oxides and Fe metal is seen.

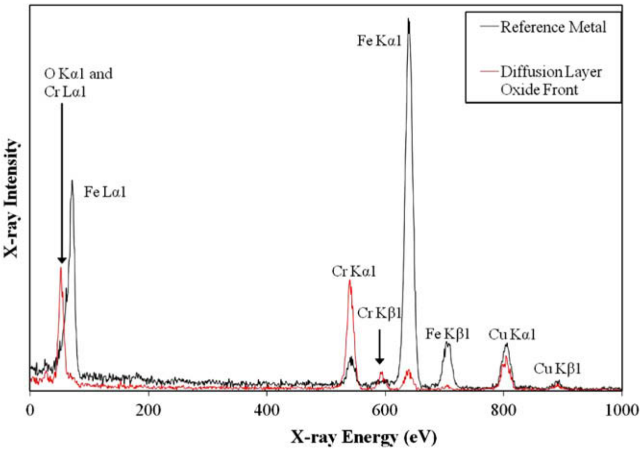

Fig. 5. EDS spectra of reference metal and region determined to be Cr_2O_3 in the diffusion layer of 9Cr ODS steel, 4-week sample.

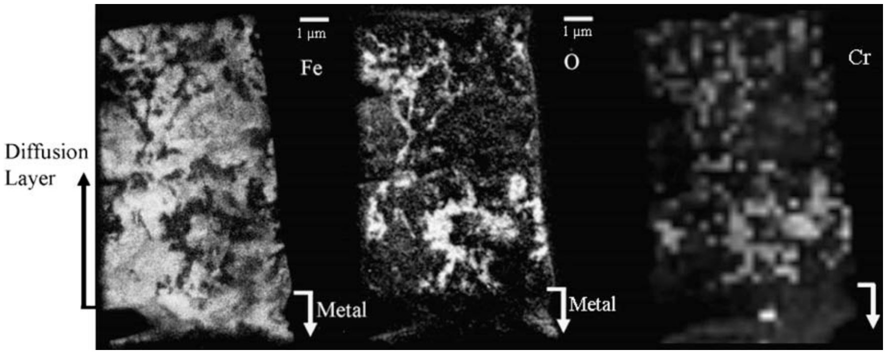

Fig. 6. Elemental maps of iron, oxygen, and chromium for the diffusion layer of 9Cr ODS steel, 2-week sample.

EDS confirms the diffraction analysis. Fig. 5 contains a pair of EDS spectra from (1) the region at the oxide front identified as Cr_2O_3 and (2) the metal. The spectrum from the oxide band reveals chromium with little iron; whereas, the reference spectrum from deep inside the metal layer reveals this region contains predominantly iron, with a small fraction of chromium and no detectable oxygen, which agrees with the diffraction analysis.

3.2.2. 9Cr ODS steel 2-weeks

A cross-sectional sample of the diffusion layer–metal interface was examined. Iron (EF), oxygen (EF), and chromium (EDS) elemental maps were also obtained for the 2-week sample and are shown in Fig. 6. As in the 4-week sample, chromium and oxygen are strongly correlated in the diffusion layer. Chromium and oxygen-rich filaments are also observed in the maps which correspond in size and morphology to the dark features seen in the diffusion layer in the SEM image in Fig. 1.

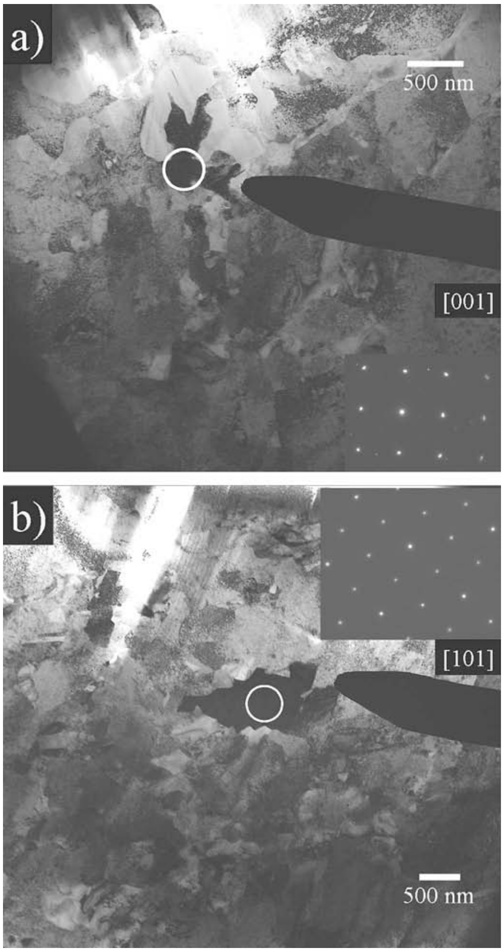

Fig. 7. TEM bright field images and corresponding diffraction patterns of (a) Fe-bcc, with a zone axis of [001] and (b) $FeCr_2O_4$, with a zone axis of [101], within the diffusion layer of 9Cr ODS steel, 2-week sample.

Fig. 7(a) shows a bright field image of an iron-containing grain in the diffusion layer, indexed as Fe-bcc. Fig. 7(b) shows a bright field image and corresponding diffraction pattern of a grain with high oxygen and chromium content. This diffraction pattern was indexed as $FeCr_2O_4$. These and several other diffraction patterns reveal that the chromium and oxygen-rich regions in the diffusion layer are $FeCr_2O_4$ and the iron-rich regions are bcc Fe.

In order to confirm these conclusions, the composition of these regions was analyzed using EDS. Fig. 8 is the EDS spectrum from the $FeCr_2O_4$ grain shown in Fig. 7(b). The spectrum reveals strong chromium peaks and smaller iron peaks. It can be seen from the spectrum that the intensity of the chromium $K_{\alpha1}$ peak is approximately twice that of the iron $K_{\alpha1}$ peak. Coupled with the diffraction analysis this indicates that the grain is $FeCr_2O_4$.

The $FeCr_2O_4$ filament-like grains found within the diffusion layer were shorter than 1.5 μm in their longest dimension, indicating that the finger-like structures consist of several grains. The Fe grains were also small, in general 1 μm or less in their longest dimension, and irregular in shape, as seen in Fig. 7(a).

While $FeCr_2O_4$ and bcc Fe were found within the diffusion layers of the 2-week and the 4-week samples, Cr_2O_3 was also found in the diffusion layer at the diffusion layer/metal interface of the 4-week sample. Between these two stages of corrosion, the thickness of the diffusion layer is reduced by a third while that of the inner

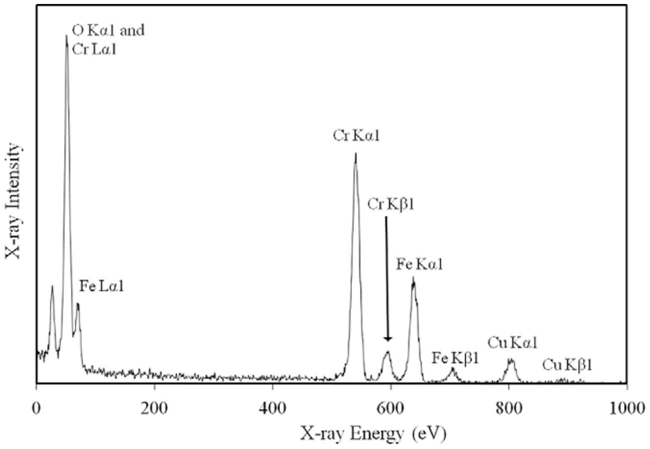

Fig. 8. EDS spectrum of $FeCr_2O_4$ grain within the diffusion layer of 9Cr ODS steel, 2-week sample.

oxide layer approximately doubles. This indicates that the overall advancement of the oxide front corrosion has slowed down, also seen by slower increase in weight gain [3,4], likely due to the development of the Cr_2O_3 band at the diffusion layer–metal interface. In parallel, an internal layer restructuring takes place between the inner oxide and diffusion layers, with large scale transfer of material. These observations agree with the microbeam synchrotron radiation fluorescence and diffraction examination of the same sample [5,8].

The evolution of the oxide layer and its relation to corrosion kinetics is a topic of great current interest, since it is clear that the structures of the protective oxide layers strongly influence corrosion kinetics. In the case of ferritic–martensitic alloys, the oxide structures are quite complex, because both anions and cations are mobile, resulting in large-scale chemical redistribution in the layer during oxide advance.

The difference between the oxide layers present after 2- and 4-week exposures is particularly striking. In the 2-week sample the diffusion layer extends a fixed distance into the metal, ahead of the oxide front, likely as a result of solid state diffusion into the base metal. The supersaturated solid solution of oxygen then decomposes into a finger-like mixture of spinel and base metal, likely by short-range lateral diffusion. As corrosion develops further, a Cr_2O_3 layer is formed at the interface, which coincides with a reduced rate of weight gain increase and oxide thickness increase. It is thought that the Cr_2O_3 layer presents a barrier for oxygen migration, effectively stopping further oxidation of the metal. This triggers a chemical rearrangement among the existing layers with little overall oxide thickness change.

It is interesting to note that other alloys have not shown similar Cr_2O_3 band development, and also that previous studies have identified superior corrosion resistance of 9Cr ODS steel compared to similar non ODS steels, thus suggesting a correlation of the oxide dispersion with corrosion resistance.

4. Conclusions

A transmission electron microscopy study was conducted of oxide layers found on 9CrODS steel after exposures to 600 °C SCW for 2- and 4-weeks. The oxide layer developed on 9CrODS exhibits three sub-layers: an outer oxide layer, an inner oxide layer, and a diffusion layer. The outer oxide layer and the inner oxide layer of the 4-week sample contain Fe_3O_4 and $FeCr_2O_4$, respectively. A filament-like structure is seen in the diffusion layer of the 2-week sample. In the 4-week 9Cr ODS steel sample, the finger-like structure still exists but the diffusion layer is thinner and a solid band of Cr_2O_3 oxide has formed at the diffusion layer/metal interface with $FeCr_2O_4$ trailing immediately behind the Cr_2O_3.

Since the appearance of the Cr_2O_3 band is coincident with a slowdown in corrosion kinetics as measured by overall oxide thickness and weight gain, it is suggested that transport in this layer may be the rate-limiting step in oxide advancement.

Acknowledgements

This research was supported by a DOE NERI Grant No. DE-FC07-06ID14744. The authors thank JAEA for providing the 9Cr ODS steel and Todd Allen, Yun Chen, and co-workers at the University of Wisconsin-Madison for supplying the corrosion samples used in this study. The authors also thank Joe Kulik and Josh Maier at the Materials Research Institute, Pennsylvania State University for help in TEM sample preparation and examination, and Jeremy Bischoff and Jamie Kunkle for helpful discussions. This publication was supported by the Pennsylvania State University Materials Research Institute NanoFabrication Network and the National Science Foundation Cooperative Agreement No. 0335765, National Nanotechnology Infrastructure Network, with Cornell University.

References

[1] US DOE Nuclear Energy Research Advisory Committee and the Generation IV International Forum, <http://nuclear.energy.gov/genIV/documents/gen_iv_roadmap.pdf>, 2002.
[2] S. Ohtuska, S. Ukai, M. Fujiwara, T. Kaito, T. Narita, Mater. Trans. 46 (2005) 487.
[3] Y. Chen, K. Sridharan, S. Ukai, T.R. Allen, J. Nucl. Mater. 359 (2006) 50.
[4] Y. Chen, K. Sridharan, S. Ukai, T.R. Allen, J. Nucl. Mater. 371 (2007) 118.
[5] A.T. Motta, A.D. Siwy, J.M. Kunkle, J.B. Bischoff, R.J. Comstock, Y. Chen, T.R. Allen, in: Proceedings of 13th International Conference on Environmental Degradation of Materials in Nuclear Systems–Water Reactor, 2007.
[6] K. Sridharan, A. Zillmer, J.R. Licht, T.R. Allen, M.H. Anderson, L. Tan, in: Proceedings of ICAPP, 2004, p. 537.
[7] A. Yilmazbayhan, A.T. Motta, R.J. Comstock, G.P. Sabol, B. Lai, Z. Cai, J. Nucl. Mater. 324 (2004) 6.
[8] J. Bischoff, A.T. Motta, R.J. Comstock, J. Nucl. Mater., these Proceedings.
[9] Lucille A. Giannuzzi, Fred A. Stevie (Eds.), Introduction to Focused ion Beams: Instrumentation: Theory, Techniques, and Practice, Springer, 2005.
[10] R.F. Egerton, Physical Principles of Electron Microscopy: An Introduction to TEM, SEM, and AEM, Springer, 2005.